UC San Diego
UC San Diego Previously Published Works

Title

Imaging and quantification of iron-oxide nanoparticles (IONP) using MP-RAGE and UTE based sequences

Permalink

Journal

ISSN

Authors

Hong, Wen
He, Qun
Fan, Shujuan
et al.

Publication Date

DOI

Copyright Information

Peer reviewed

Imaging and Quantification of Iron-Oxide Nanoparticles (IONP) Using MP-RAGE and UTE based sequences

Wen Hong[1,2,*], **Qun He**[1,3,*], **Shujuan Fan**[1], **Michael Carl**[4], **Hongda Shao**[1], **Jun Chen**[1], **Eric Y Chang**[1,5], and **Jiang Du**[1]

[1]Department of Radiology, University of California, San Diego, CA

[2]Department of Radiology, China-Japan Friendship Hospital, Beijing, China

[3]Ningbo Jansen NMR Technology Co., Ltd., Cixi, Zhejiang Province, China

[4]Applied Science Lab, GE Healthcare, San Diego, CA

[5]Radiology Service, VA San Diego Healthcare System, San Diego, CA

Abstract

Purpose—To investigate two-dimensional (2D) and 3D ultrashort echo time (UTE) and 3D magnetization-prepared rapid gradient-echo (MP-RAGE) sequences for the imaging of iron-oxide nanoparticles (IONP).

Methods—The phantoms composed of tubes filled different IONP concentrations ranging from 2 to 45 mM. The tubes were fixed in an agarose gel phantom (0.9% by weight). Morphological imaging was performed with 3D MP-RAGE, 2D UTE, 2D adiabatic inversion recovery prepared UTE (2D IR-UTE), 3D UTE with Cones trajectory (3D Cones), and 3D IR-Cones sequences. Quantitative assessment of IONP concentration was performed via $R2^*$ ($1/T2^*$) and $R1$ ($1/T1$) measurements using a 3T scanner.

Results—The 3D MP-RAGE sequence provides high contrast images of IONP with concentration up to 7.5 mM. Higher IONPs concentration up to 37.5 mM can be detected with the UTE sequences, with the highest IONP contrast provided by the 3D IR-Cones sequence. A linear relationship was observed between $R2^*$ and IONPs concentration up to ~45 mM, and between $R1$ and IONPs concentration up to ~30 mM.

Conclusion—The clinical 3D MP-RAGE sequence can be used to assess lower IONP concentration up to 7.5 mM. The UTE sequences can be used to assess higher IONP concentration up to 45 mM.

Keywords

IONP; iron oxide nanoparticles; MRI; UTE; Cones; MP-RAGE

---

*Corresponding Author: Jiang Du, Ph.D. University of California, San Diego, Department of Radiology, 200 West Arbor Drive, San Diego, CA 92103-8226, Phone (619) 471-0519, Fax (619) 471-0503, Word count: 3362, jiangdu@ucsd.edu.

the first two authors have equal contributions

Introduction

Iron is an essential element for life and is involved in a number of integral biologic processes, including the production of hemoglobin and myoglobin, transporting oxygen from the lungs to other tissues, developing and maintaining the normal function of myelin, and multiple enzymatic processes [1-5]. However, iron is also a potentially toxic substance. If iron stores exceed the amount that the body can chelate, free iron will accumulate. This unbound iron promotes intracellular transformation of hydrogen peroxide into free radical, resulting in membrane lipid peroxidation, cellular injury, progressive fibrosis, and ultimately organ dysfunction [2, 6-7].

Many postmortem and in vivo studies have revealed that gender and age-related differences exist with regard to total iron content, and that the distribution of iron in the body can differ greatly, dependent on the particular organ and cell type [2,7-11]. There are several types of diseases that may lead to very high iron content in the human body. Liver iron overload is associated with hemosiderosis, thalassemia, and sideroblastic anemia. Normal liver iron concentration values are up to 1.8 mg/g dry weight (approximately 8.4 mM in fresh tissue, supposing a dry to wet ratio of 4 and a liver density of 1.05 mg/mL) [12]. Patients with sickle cell anemia or thalassemia major receive frequent blood transfusions and may have very high liver iron concentrations, reported up to 15.99 mg/g wet weight (equivalent to ~277.7 mM) [13]. It is recommended to maintain a liver iron concentration of 3.2–7 mg/g dry weight (approximately 15-32.8 mM in fresh tissue) for chelation therapy in patients with thalassemia major[12]. In the heart, the average iron concentration was 1.14 mg/g wet weight (range = 0.77–1.50 mg/g, or 15.1-29.5 mM) in patients with thalassemia, as compared to a normal value of 0.06 mg/g (range = 0.02–0.12 mg/g, or 0.4-2.4 mM) [14]. In patients with rheumatoid arthritis, iron content in synovial tissue ranged from 0.04-0.45 mg/g wet weight (or 0.8-8 mM) [15]. Hemophilia patients may have 20 times or higher iron concentration in the knee joint due to continuous bleeding and subsequent iron accumulation [16-18]. People with hemochromatosis may have iron deposits in the pituitary gland, pancreas, heart muscle, and liver, with liver iron concentration up to 22 mg/g dry weight (equivalent to approximately 103 mM in fresh tissue) [18]. Iron overload can affect a number of organs besides the central nervous system, including the liver, pancreas, myocardium, endocrine glands, and musculoskeletal structures. This can lead to cirrhosis of the liver, diabetes mellitus, cardiomyopathy, hypogonadotropic hypogonadism, and polyarthropathy, respectively [2,19-24].

A sensitive, reproducible, reliable, and non-invasive method to detect and measure iron in vivo would be of great clinical utility. The measurement of iron levels is paramount for the diagnosis of various diseases and for predicting the outcomes of some diseases. In addition, it is used to monitoring chelation therapy for the treatment of iron overload syndromes and for understanding some disease mechanisms. Biopsy is still considered the "gold standard" for assessing tissue iron level, however it is an invasive method which carries the risk of serious complications. Furthermore, iron deposition may be heterogeneous in some organs, causing variability in tissue sampling and histologic interpretation [2, 19-21]. Serum measurements, including iron, transferrin, and ferritin, are simpler, but are considered indirect methods to assess iron burden at the parenchymal level. Accuracy with serum

measurements are also impacted by hepatic function, citrate and ascorbate status, and the presence of inflammatory conditions or malignant neoplasms [2,24].

Recently, magnetic resonance (MR) imaging has emerged as a method to estimate tissue iron levels, both in vitro and in vivo. Iron has endogenous paramagnetic characteristics, and causes shortened T1, T2, and T2* relaxation times as well as phase and susceptibility changes by affecting the magnetic environment of water protons. MR imaging can be used to qualitatively assess and quantify iron levels in vivo using both standard and specially designed techniques [1-2, 25-27]. Previous studies have focused on gradient recalled echo (GRE) sequences to investigate the relationship between iron concentration and R2* (1/T2*) [1-2, 24]. However, these sequences are less effective in tissues with high iron concentration in patients with thalassemia, hemophilia, hemochromatosis, rheumatoid arthritis, etc. The high iron concentration leads to shortening of T2*, which may cause significant signal loss when imaged with conventional clinical MR sequences.

Ultrashort echo time (UTE) sequences can detect signal from short T2 species with T2*s of a few hundred microseconds or less. UTE-based sequences have shown great success in detecting and imaging short T2/T2* tissues or tissue components [28-31]. Several groups have published techniques on IONP imaging and quantification using sweep imaging with Fourier transformation (SWIFT) [32-34], which is one type of UTE sequences but has with much shorter effective TE. IONP concentration can be measured via T1 measurement using varying flip angle SWIFT (VFA-SWIFT) [33] and SWIFT Look-Locker method [34]. However, these studies are performed on high performance NMR spectrometers. High contrast imaging and quantification of high level IONP on a clinical whole-body MR scanner using UTE sequences remain to be investigated. Such a technique may have great potential in monitoring the treatment of diseases such as thalassemia, hemophilia, hemochromatosis, or rheumatoid arthritis, or in magnetic nanoparticle based hyperthermia and drug delivery.

Adiabatic inversion recovery prepared UTE (IR-UTE) sequences have been employed to image short T2 tissues or tissue components with efficient suppression of longer T2 tissues or tissue components [35-37]. More recently, 3D UTE with Cones trajectory (3D UTE Cones) and its combination with adiabatic inversion preparation (3D IR-Cones) have been developed for fast volumetric imaging of short T2 tissues [38]. The three-dimensional magnetization-prepared rapid gradient-echo (3D MP-RAGE) sequence can generate high tissue contrast and provides high spatial resolution in a short scan time [39, 40]. The purpose of this study is to investigate the feasibility of high contrast imaging of iron with 3D MP-RAGE sequence for low iron oxide nanoparticles (IONP) concentration, and 2D IR-UTE and 3D IR-Cones sequences for high IONP concentration. Quantitative assessment of IONP concentration was investigated by measuring R2* and R1 of a series of IONP phantoms using 2D/3D UTE and IR-UTE sequences on a clinical 3T MR scanner.

Materials and Methods

An iron phantom was prepared for this study. The phantom was composed of tubes filled with 2 mL of Feridex I.V. solution (ferumoxides injectable solution, Berlex Laboratories,

Wayne, NJ) with seven different concentrations of 2, 7.5, 15, 22.5, 30, 37.5 and 45 mM. Since T2* is strongly affected by susceptibility, the tubes were put in a cylinder container (10 cm in diameter) filled with agarose gel (0.9% by weight) with the longitudinal direction of the tubes placed parallel to the B_0 field such that the susceptibility artifact was minimized. The angular dependence of R1/R2* measurements was not investigated in this study.

MR imaging of phantoms was performed on a 3T SignaHDxt scanner (GE Healthcare Technologies, Milwaukee, WI). Morphological imaging of IONP was performed using six different sequences, including 3D GRE, 3D MP-RAGE, 2D UTE, 2D IR-UTE, 3D Cones and 3D IR-Cones sequences. The basic imaging parameters were listed in Table 1 for all six sequences.

In order to quantify IONP concentration, R2* (1/T2*) was measured with the 2D UTE and IR-UTE sequences as well as the 3D Cones and 3D IR-Cones sequences. Imaging parameters were similar to those used above for morphological imaging except repeated acquisitions with a series of TEs (TEs = 32 μs, 45 μs, 55 μs, 65 μs, 75 μs, 85 μs, 0.1, 0.15, 0.2, 0.25, 0.35, 0.5, 0.75, 1.0, 1.5, 2, 3 ms) for T2* measurement based on the following single exponential signal decay model:

$$S(TE) = S_0 \times e^{-TE/T2^*} + C \quad (1)$$

where C accounts for background noise, including pseudo-noise associated with streak artifacts in 2D radial UTE and 3D Cones data acquisitions.

T1 measurement was also performed to quantify IONP concentration. Quantification of T1 requires the use of UTE sequences because high IONP concentration corresponds to very short T2*. 2D saturation recovery UTE (2D SR-UTE) has been shown to provide reliable measurement of T1 of cortical bone, and was used here to quantify T1 of various IONP phantoms. In SR-UTE, a non-selective 90° square pulse with duration of 256 μs (which is limited by the RF system) was followed by a large crusher gradient to saturate signals from both long and short T2 species. 2D UTE acquisitions with progressively increasing saturation recovery times (TSRs) were then used to detect the recovery of longitudinal magnetization. Imaging parameters were similar to those used above for morphological imaging except a long TR of 1000 ms and a series of TSRs of 7.8, 10, 12.5, 15, 22.5, 30, 50, 80, 120, 180, 250, 400, 600 ms. The single exponential signal recovery model shown below was used to fit T1 [31]:

$$S(\text{TSR}) = S_0 \times [1 - (1 - k) \times e^{-TSR/T1}] + C \quad (2)$$

where k accounts for the residual fraction of the longitudinal magnetization after a nominal 90° pulse.

The saturation recovery approach with 3D imaging is too time-consuming, even when using optimized 3D Cones sequences. To save time, we employed 3D Cones with variable TR (3D Cones-VTR) approach to quantify T1. Imaging parameters were similar to those used above for morphological imaging except a series of TRs of 4.7, 6, 8, 10, 12.5, 15, 20, 25, 37.5, 50, 75 and 100 ms. The transverse magnetization for a steady-state UTE acquisition can be written as [31]:

$$M_{xy}^{\mathrm{UTE}} \alpha f_{xy}(b_1(t), T_1, T_2^*) \times (1 - e^{-TR/T_1}) \times e^{-TR/T_2^*} / (1 - f_z(b_1(t), T_1, T_2^*) \times e^{-TR/T_1})) \quad (3)$$

Where f_{xy} and f_z describe the behavior of the transverse magnetization and longitudinal magnetization, respectively, as a function of the pulse b1(t) as well as the T2* and T1 relaxation times. For the 3D Cones and IR-Cones sequences, the duration of the excitation pulse (i.e., 52 μs, 20° rectangular pulse) is significantly shorter than both T2* and T1 of IONP phantom (including those with the highest IONP concentration), therefore relaxation effects during RF excitation could be ignored as a first order approximation. Therefore, the above equation can be simplified as below:

$$M_{xy}^{\mathrm{UTE}}(TR, TE=8\mu s) \propto M_{0,,xy}^{UTE} \times f_{xy} \times (1 - e^{-TR/T_1}) \times e^{-TE/T_2^*} / (1 - f_z \times e^{-TR/T_1})) \quad [4]$$

Image Analysis

The analysis algorithm was written in Matlab (The MathWorksInc., Natick, MA, USA) and was executed offline on the DICOM images obtained by the protocols described above. Contrast to noise ratio (CNR) was used to evaluate all the sequences for morphological imaging of IONP. CNR was measured as the signal difference between IONP phantom and nearby agarose divided by the standard deviation of background signal in air. T2* was estimated using Eq. 1 for the 2D UTE, 2D IR-UTE, 3D Cones and 3D IR-Cones approaches. T1 was estimated using Eq. 2 for the 2D SR-UTE approach and Eq.4 for the 3D Cones-VTR approach. The fitted R2* (1/T2*) and R1 (1/T1) values were plotted against IONP concentration to show their relationship.

Results

Figure 1 shows a phantom containing tubes with different IONP concentrations as well as images using 3D GRE, 3D MP-RAGE, 2D UTE, 2D IR-UTE, 3D Cones and 3D IR-Cones sequences. The locations of the tubes can be identified using all sequences. The 3D MP-RAGE sequence shows high contrast images for IONP concentrations up to 7.5 mM.When IONP concentration is above 7.5 mM, the 3D MP-RAGE sequence shows near zero signal with strong dipolar artifacts. The 2D UTE and IR-UTE sequences can access IONP concentration up to 37.5 mM, while the 3D Cones and IR-Cones sequences can access IONP up to 45 mM. Table 2 shows the CNR measurements for all IONP phantoms and all

sequences. The 3D IR-Cones sequence provides the best contrast throughout the range of IONP concentrations used in this study.

Figure 2 shows representative 3D Cones and 3D IR-Cones imaging of the IONP phantom with a series of TEs, as well as single-component T2* fitting curves of various IONP concentrations. Excellent curve fitting was obtained for all cases, especially for IONP concentrations in the range of 7.5 – 37.5 mM. Some distortion was observed for high IONP concentration of 45 mM. The 2D IR-UTE imaging shows similar image quality and T2* curve fitting for IONP concentration up to 30 mM. However, the 2D UTE sequence shows too strong distortion when the IONP concentration is above 15 mM likely due to eddy current effects associated with 2D slice-selective half-pulse excitation.

Figure 3 shows R2* values plotted against IONP concentrations, where R2* was measured with 2D UTE, 2D IR-UTE, 3D Cones and 3D IR-Cones sequences, respectively. The data shows that R2* and the IONP concentration have a linear relationship up to 15 mM for 2D UTE ($R^2 = 0.9537$), up to 30 mM for 2D IR-UTE ($R^2 = 0.9233$), up to 37.5 mM for 3D Cones ($R^2 = 0.9922$), and up to 45 mM for 3D IR-Cones ($R^2 = 0.9971$). The 3D IR-Cones sequence provides the most accurate IONP quantification via R2* measurement.

Figure 4 shows representative 3D Cones imaging of the IONP phantom with a series of TRs, as well as single-component T1 fitting curves of various IONP concentrations. Excellent curve fitting was obtained for all cases with IONP concentrations up to 30 mM. Some distortion was observed for IONP concentration above 37.5 mM.

Figure 5 shows R1 values plotted against IONP concentrations, where R1 was measured with 2D SR-UTE and 3D Cones-VTR sequences, respectively. The data shows that R1 and the IONP concentration up to 30 mM have a linear relationship.

Discussion

Measurement of tissue iron level using MR imaging has many advantages, including its noninvasive nature, convenience, and strong repeatability. Various portions of the body can be easily interrogated and the information can potentially be useful for diagnosis, monitoring and assessing response to therapy, and for understanding the pathogenesis in iron-related diseases.

To detect and measure the concentration of iron with MR, there are many important technical factors that need to be considered. For instance, many relaxation time measurements exist including R1 [1/T1], R2 [1/T2] and R2* [1/T2*], each with individual challenges for implementation. In addition, the selection of a scan sequence that is able to obtain an echo time as fast as possible is important to capture the rapidly decaying signal. Field strength and the method of image post-processing to improve artifacts are also important considerations. In this paper, our focus was on obtaining high quality images using short echo times that are based on MP-RAGE and UTE sequences.

Our study shows that improved iron contrast can be achieved with the 2D IR-UTE and 3D IR-Cones sequences. This is consistent with the results published by Wang et al., who

demonstrated that the sweep imaging with Fourier transformation (SWIFT) sequence with long T2 suppression provided improved CNR between INOP and the long T2 species [28]. The quantitative measurements are also consistent with recently published results based on the SWIFT approaches. Wang et al. measured T1 values of various IONP concentrations from 1 to 7 mM using varying flip angle sweep imaging with Fourier transformation (VFA-SWIFT) and 3D SPGR with variable flip angles (VFA-SPGR) sequences on a 7T MR scanner [29]. They found an excellent linear relationship between R1 and IONP concentration. Zhang et al. employed the SWIFT sequence combined with the Look-Locker method to map T1 of IONP in high concentrations [30]. They found that the SWIFT Look-Locker sequence could accurately measure T1 of IONP concentrations up to 53.6 mM. The SWIFT sequence can access significantly higher IONP concentrations (~53.6 Mm vs. ~37.5 Mm) than the 3D Cones and IR-Cones sequences likely due to its shorter effective TE (near zero). Although the 3D Cones and 3D IR-Cones sequences have a minimal nominal TE of 32 μs, the effective TE is expected to be much longer due to ramp sampling.

Previous authors have demonstrated that image quality and contrast are better using the 3D MP-RAGE sequence compared with conventional T1-weighted spin echo sequences (36). We have used the 3D MP-RAGE sequence to obtain T1-weighted images and determined the relationship between R2* and different concentrations of IONP. We have found that excellent image quality can be achieved using this sequence for low concentrations of IONP (Fig 1). In our study we have also used the 2D UTE, 2D IR-UTE, 3D Cones and 3D IR-Cones sequences for quantitative measurements of IONP. Using all four sequences, an approximately linear relationship was visualized for IONP concentrations ranging from ~2 to ~37.5 mM.

Due to its electromagnetic properties, iron causes T2 shortening and signal is particularly difficult to detect using T2-weighted MR images. The higher the iron concentration, the shorter the T2 value. Using conventional MR sequences with limitations in the lowest achievable TE value, there is insufficient signal from the upper range of iron concentrations used in our study. Specifically, signal intensity and contrast is too low to distinguish concentrations above 7.5 mM from the background. This highlights the importance of echo time selection, which should be as short as possible. UTE sequences can detect signal from short T2 species with T2*s of a few hundred microseconds. We have demonstrated that UTE-based sequences show great success in detecting and imaging short T2/T2* objects. Our data shows that the R2* and the IONP concentration ranging from 2 to 37.5 mM have a linear relationship and images are better compared with conventional sequences.

In general, the 3D Cones and IR-Cones sequences outperform the 2D UTE and IR-UTE sequences in quantitative assessment of IONP. The 2D UTE sequence shows a near linear relationship between T2* and IONP concentration up to 15 mM, while the 3D Cones sequence shows an excellent linear relationship between T2* and IONP concentration up to 37.5 mM. The same trend was also observed between the 2D IR-UTE and 3D IR-Cones sequences. This difference is likely due to eddy currents, which affect the 2D UTE sequences much more than the 3D Cones sequences [38]. The 2D UTE sequences employ half-pulse for slice selective excitation, which is known to be sensitive to eddy currents [41]. The 3D Cones sequences employ a short rectangular pulse for non-selective excitation,

eliminating slice-selective gradients and the associated eddy currents. Furthermore, the 2D IR-UTE and 3D IR-Cones sequences perform better than the 2D UTE and 3D Cones sequences, respectively. This is due to the suppression of long T2 signals, with reduction of the associated eddy current.

Increased error was observed in the T1 measurements of IONP above 30 mM. IONP shortens not only T2* but T1. With a concentration of 30 mM, T1 was reduced to 7.8 ms while T2* was reduced to ~0.12 ms. When IONP concentration was increased to 37 mM, T1 was further reduced to ~4.3 ms. The minimum TR of the Cones sequence was around 4.7 ms. It is technically difficult to accurately measure T1 around or below the minimum TR using the variable TR approach. T2* is likely a better option to quantitatively evaluate IONP above 30 mM.

There are several limitations of this study. First, R2* and R1 were measured only for phantoms where iron tubes were aligned parallel to the B0 field, and thus susceptibility effect was minimized. The angular dependence of R2*/R1 vs. iron concentration remains to be investigated. The sensitivity to B0 and B1 inhomogeneity is not investigated. The UTE sequences, especially the 3D UTE sequences, should be less sensitive to B0 inhomogeneity than conventional gradient echo sequences due to the ultrashort TEs and non-selective excitation. The variable TR approach, similar to the conventional inversion recovery, variable flip angle and Look-Locker methods, is subject to errors due to B1 inhomogeneity. B1 mapping will improve T1 measurements. Second, scan time optimization was not considered in this phantom study. The total scan time can be greatly reduced by using two to three sets of interleaved multi-echo 3D Cones sequences for fast volumetric R2* measurement. R1 can be measured with two to four TRs for fast T1 mapping. Third, in vivo applications remain to be investigated. It is likely that in vivo quantification of IONP will be much more complicate as there are many factors affecting T1 and T2*. Improved accuracy is expected for high IONP level where iron is the dominating factor. Clearly more in vivo studies are required, especially using whole-body clinical MR scanners. However, results from this study should provide the basics on iron quantification, as well as the upper limit of iron concentration which can be reliably measured with UTE sequences on clinical MR scanners.

Conclusions

For qualitative assessment of iron-laden tissues, high quality images can be generated using the 3D MP-RAGE sequence only for low concentrations of iron whereas the UTE-based sequences, especially 2D IR-UTE and 3D IR–Cones sequences, allow high quality images to be generated over a range of low to high IONP concentrations up to 45 mM. IONP concentrations up to 37.5 mM can be measured with R2* or R1 measurement using a clinical 3T MR scanner.

Acknowledgments

References

1. Bartzokis G. Alzheimer's disease as homeostatic responses to age-related myelin breakdown. Neurobiol Aging. 2011; 32(8):1341–1371. [PubMed: 19775776]

2. Sirlin CB, Reeder SB. Magnetic resonance imaging quantification of liver iron. Magn Reson Imaging Clin N Am. 2010; 18(3):359–381. [PubMed: 21094445]

3. Quintana C, Bellefqih S, Laval JY, et al. Study of the localization of iron, ferritin, and hemosiderin in Alzheimer's disease hippocampus by analytical microscopy at the subcellular level. J Struct Biol. 2006; 153(1):42–54. [PubMed: 16364657]

4. Stankiewicz J, Panter SS, Neema M, et al. Iron in chronic brain disorders: imaging and neurotherapeutic implications. Neurotherapeutics. 2007; 4(3):371–386. [PubMed: 17599703]

5. Todorich B, Pasquini JM, Garcia CI, et al. Oligodendrocytes and myelination: the role of iron. Glia. 2009; 57(5):467–478. [PubMed: 18837051]

6. Bartzokis G. Age-related myelin breakdown: a developmental model of cognitive decline and Alzheimer's disease. Neurobiol Aging. 2004; 25(1):5–18. [PubMed: 14675724]

7. Bartzokis G, Tishler TA, Shin ILS, et al. Brain ferritin iron as a risk factor for age at onset in neurodegenerative diseases. Ann N Y Acad Sci. 2004; 1012(1):224–236. [PubMed: 15105269]

8. Hallgren B, Sourander P. The effect of age on the non-haemin iron in the human brain. J Neurochem. 1958; 3(1):41–51. [PubMed: 13611557]

9. Haacke EM, Cheng NYC, House MJ, et al. Imaging iron stores in the brain using magnetic resonance imaging. Magn Reson Imaging. 2005; 23(1):1–25. [PubMed: 15733784]

10. Bartzokis G, Lu PH, Tishler TA, et al. Myelin breakdown and iron changes in Huntington's disease: pathogenesis and treatment implications. Neurochem Res. 2007; 32(10):1655–1664. [PubMed: 17484051]

11. Bartzokis G, Tishler TA, Lu PH, et al. Brain ferritin iron may influence age-and gender-related risks of neurodegeneration. Neurobiol Aging. 2007; 28(3):414–423. [PubMed: 16563566]

12. Taher AT, Musallam KM, Inati A. Iron overload: consequences, assessment, and monitoring. Hemoglobin. 2009; 33(S1):S46–57. [PubMed: 20001632]

13. Brittenham GM, Cohen AR, McLaren CE, Martin MB, Griffith PM, Nienhuis AW, Young NS, Allen CJ, Farrell DE, Harris JW. Hepatic iron stores and plasma ferritin concentration in patients with sickle cell anemia and thalassemia major. Am J Hematol. 1993; 42:81–85. [PubMed: 8416302]

14. Ghugre NR, Enriquez CM, Gonzalez I, Nelson MD, Coates TD, Wood JC. MRI detects myocardial iron in the human heart. Magn Reson Med. 2006; 56(3):681–686. [PubMed: 16888797]

15. Mowat AG, Hothersa Te. Nature of Anaemia in Rheumatoid Arthritis .8. Iron Content of Synovial Tissue in Patients with Rheumatoid Arthritis and in Normal Individuals. Ann Rheum Dis. 1968; 27(4):345–351. [PubMed: 5666675]

16. Roosendaal G, Vianen ME, Wenting MJG, van Rinsum AC, van den Berg HM, Lafeber FPJG, Bijlsma JWJ. Iron deposits and catabolic properties of synovial tissue from patients with haemophilia. J Bone Joing Surg. 1998; 80:540–545.

17. vanVulpen LFD, Roosendaal G, van Asbeck BS, Mastbergen SC, Lafeber FPJG, Schutgens REG. The detrimental effects of iron on the joint: a comparison between haemochromatosis and haemophilia. J Clin Pathol. 2015; 68(8):592–600. [PubMed: 25897098]

18. Batts KP. Iron overload syndromes and the liver. Modern Pathology. 2007; 20:S31–S39. [PubMed: 17486050]

19. Wood JC. Magnetic resonance imaging measurement of iron overload. Curr Opin Hematol. 2007; 14(3):183. [PubMed: 17414205]

20. Wood JC. Diagnosis and management of transfusion iron overload: the role of imaging. Am J Hematol. 2007; 82(S12):1132–1135. [PubMed: 17963249]

21. Wood JC, Ghugre N. Magnetic resonance imaging assessment of excess iron in thalassemia, sickle cell disease and other iron overload diseases. Hemoglobin. 2008; 32(1-2):85–96. [PubMed: 18274986]

22. Wood JC. Cardiac complications in thalassemia major. Hemoglobin. 2009; 33(S1):S81–S86. [PubMed: 20001637]

23. Ghugre NR, Gonzalez-Gomez I, Butensky E, et al. Patterns of hepatic iron distribution in patients with chronically transfused thalassemia and sickle cell disease. Am J Hematol. 2009; 84(8):480–483. [PubMed: 19536851]

24. Wood JC. Impact of iron assessment by MRI. Hematology Am Soc Hematol Educ Program. 2011; 2011(1):443–450. [PubMed: 22160072]

25. Hoopes PJ, Petryk AA, Gimi B, Giustini AJ, Weaver JB, Bischof J, Chamberlain R, Garwood M. In vivo imaging and quantification of iron oxide nanoparticle update and biodistribution. SPIE Medical Imaging. 2012:83170R.

26. Zhang, J., Ring, HL., Hurley, K., Shao, Q., Klein, ND., Haynes, C., Bischof, J., Garwood, M. Using SWIFT T1 mapping to quantify iron oxide nanoparticles uptake and biodistribution in organs in-vivo. Proceedings of ISMRM 23rd Annual Meeting; Toronto, Canada. June 2015; p. 694

27. Zhang, J., Petryk, AA., Reeves, R., Idiiyatullin, D., Ring, HL., Hoopes, PJ., Garwood, M. In-vivo quantification of iron oxide nanoparticles at high concentration in a murine breast tumor model using positive contrast. Proceedings of ISMRM 23rd Annual Meeting; Toronto, Canada. June 2015; p. P225

28. Du J, Carl M, Bae WC, et al. Dual inversion recovery ultrashort echo time (DIR-UTE) imaging and quantification of the zone of calcified cartilage (ZCC). Osteoarthritis and Cartilage. 2013; 21(1): 77–85. [PubMed: 23025927]

29. Du J, Bydder GM. Qualitative and quantitative ultrashort TE MRI of cortical bone. NMR Biomed. 2013; 26(5):489–506. [PubMed: 23280581]

30. Du J, Hermida JC, Diaz E, et al. Assessment of cortical bone with clinical and ultrashort echo time sequences. Magn Reson Med. 2013; 70(3):697–704. [PubMed: 23001864]

31. Robson MD, Gatehouse PD, Bydder M, et al. Magnetic resonance: an introduction to ultrashort TE (UTE) imaging. J Comput Assist Tomogr. 2003; 27(6):825–846. [PubMed: 14600447]

32. Wang L, Tang W, Zhen Z, Chen H, Xie J, Zhao Q. Improving detection specificity of iron oxide nanoparticles (IONPs) using the SWIFT sequence with long T(2) suppression. Magn Reson Imaging. 2014; 32:671–678. [PubMed: 24666573]

33. Wang L, Corum CA, Idiyatullin D, Garwood M, Zhao Q. T1 estimation for aqueous iron oxide nanoparticle suspensions using a variable flip angle SWIFT sequence. Magn Reson Med. 2013; 71:1982–1988.

34. Zhang J, Chamberlain R, Etheridge M, Idiyatullin D, Corum C, Bischof J, Garwood M. Quantifying iron-oxide nanoparticles at high concentration based on longitudinal relaxation using a three-dimensional SWIFT Look-Locker sequence. Magn Reson Med. 2014; 71:1982–1988. [PubMed: 24664527]

35. Du J, Carl M, Bydder M, Takahashi A, Chung CB, Bydder GM. Qualitative and quantitative ultrashort echo time (UTE) imaging of cortical bone. J Magn Reson. 2010; 207:304–311. [PubMed: 20980179]

36. Du J, Bydder M, Takahashi AM, Carl M, Chung CB, Bydder GM. Short T2 contrast with three-dimensional ultrashort echo time imaging. Magn Reson Imaging. 2011; 29:470–82. [PubMed: 21440400]

37. Horch R, Gochberg D, Nyman J, Does M. Clinically-compatible MRI strategies for discriminating bound and pore water in cortical bone. Magn Reson Med. 2012; 68:1774–1784. [PubMed: 22294340]

38. Carl M, Bydder GM, Du J. UTE imaging with simultaneous water and fat signal suppression using a time-efficient multi-spoke inversion recovery pulse sequence. Magn Reson Med. 2016; 76(2): 577–582. [PubMed: 26309221]

39. Mugler JP, Brookeman JR. Three-dimensional magnetization-prepared rapid gradient echo imaging (3D MP RAGE). Magn Reson Med. 1990; 15(1):152–157. [PubMed: 2374495]

40. Brant-Zawadzki M, Gillan GD, Nitz WR. MP RAGE: a three-dimensional, T1-weighted, gradient-echo sequence--initial experience in the brain. Radiology. 1992; 182(3):769–775. [PubMed: 1535892]
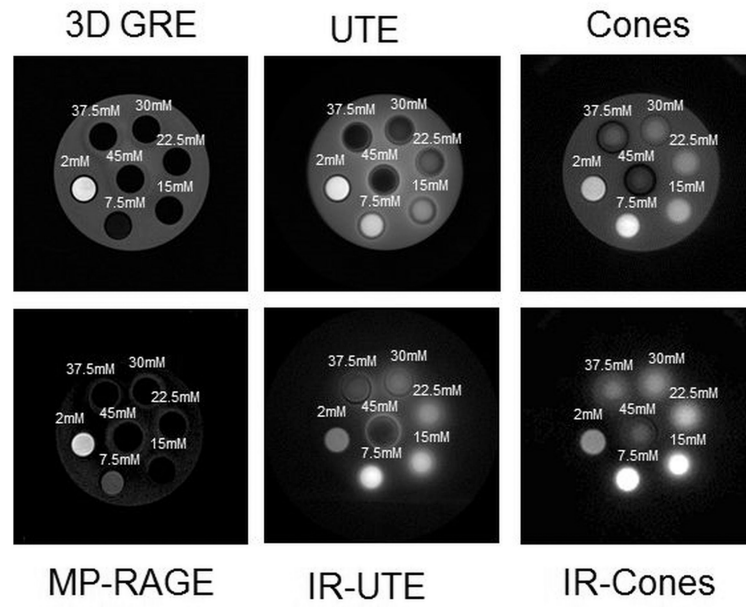
41. Lu A, Daniel BL, Pauly JM, Pauly KB. Improved slice selection for R2* mapping during cryoablation with eddy current compensation. J Magn Reson Imaging. 2008; 28:190–198. [PubMed: 18581340]
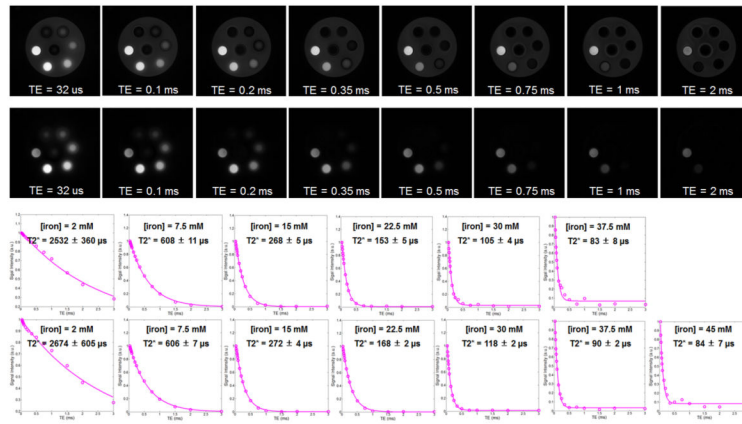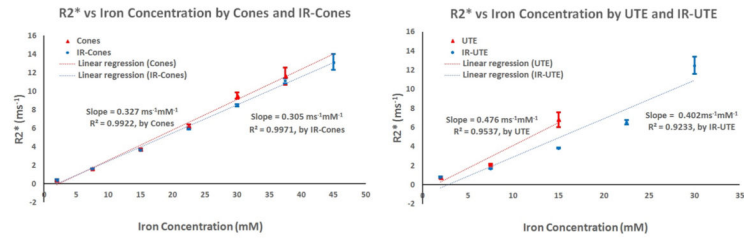
Figure 1.
Morphological images of iron-oxide nanoparticle phantoms. Using 3D GRE, 3D MP-RAGE, 2D-UTE, 2D IR-UTE, 3D Cones, and 3D IR-Cones sequences, positive contrast can be appreciated up to concentrations of 2, 7.5, 22.5, 37.5, 45, and 45 mM, respectively. With the highest concentration tube used (45 mM), the IR-Cones sequence yields the greatest signal.

Figure 2.
Selected morphological images of IONP tubes using 3D Cones (1st row) and 3D IR-Cones (2nd row) sequences with single-component T2* curve fitting for different IONPs concentrations acquired with 3D Cones (3rd row) and 3D IR-Cones (4th row) sequences.

Figure 3.
R2* (1/T2*) values are plotted versus the concentration of iron by using T2* as determined using 2D (2D-UTE and 2D IR-UTE) and 3D (3D Cones and 3D IR-Cones) measurements for determining iron concentration.
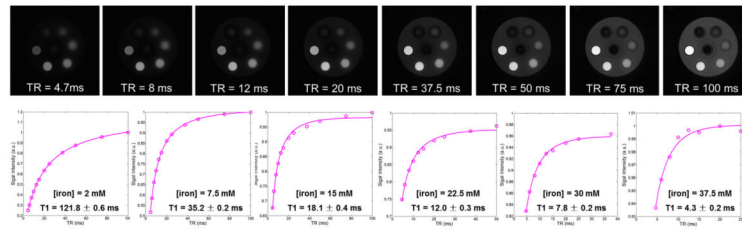
Figure 4.
Selected 3D Cones images of IONP tubes acquired with variable TRs ranging from 4.7 ms to 100 ms (upper row) and single-component T1 fitting curves for different iron concentrations (lower row). Excellent curve fitting is seen up to a concentration of 30 mM.
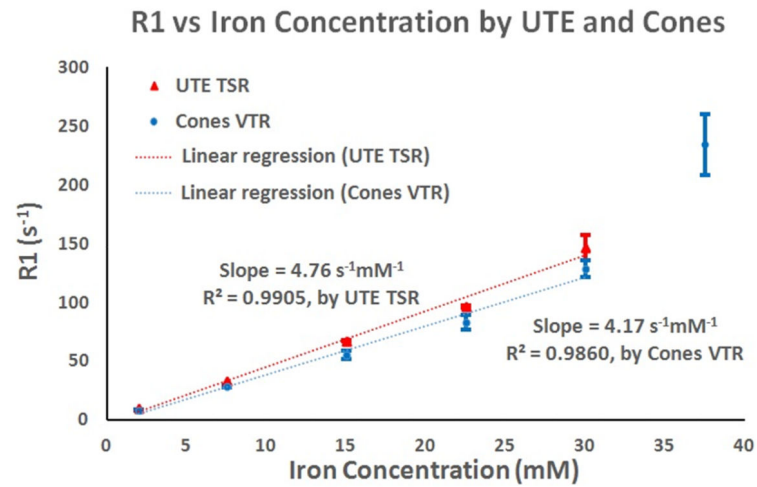
Figure 5.
R1 (1/T1) values are plotted versus the concentration of iron by using T1 as determined using 2D SR-UTE and 3D Cones-VTR sequences. The data shows that the R1 and the iron concentration ranging up to 30 mM have a good linear relationship.

Table 1

Imaging parameters for 3D GRE, 3D MP-RAGE, 2D UTE, 2D IR-UTE, 3D Cones and 3D IR-Cones sequences.

Sequences	TR (ms)	TE (ms)	T1 (ms)	FOV (cm)	Matrix	#slice	Thickness (mm)	BW (Hz/Pixel)	Flip Angle	Scan Time (min:sec)
3D MP-RAGE	6.79	1.92	80	18	256 × 256	32	2	122	12°	1:48
3D GRE	6.79	1.92	-	18	256 × 256	32	2	122	12°	1:12
2D UTE	300	0.01	-	16	128 × 128	1	2	977	60°	2:02
2D IR-UTE	300	0.01	110	16	128 × 128	1	2	977	60°	2:02
3D Cones	6.2	0.01	-	16	128 × 128	20	2	1953	20°	1:16
3D IR-Cones	100	0.01	45	16	128 × 128	20	2	1953	20°	1:49

CNR measurements for all iron-oxide nanoparticle phantoms using 3D GRE, 3D MP-RAGE, 2D UTE, 2D IR-UTE, 3D Cones, 3D IR-Cones sequences.

[Fe] (mM)	2	7.5	15	22.5	30	37.5	45
3D GRE	105.11	-37.88	x	x	x	x	x
MP-RAGE	82.79	12.47	x	x	x	x	x
UTE	112.18	86.27	31.15	-12.78	-43.13	-65.31	-65.91
IR-UTE	64.65	195.77	169.03	102.87	49.94	9.79	-12.71
Cones	412.78	489.65	358.59	226.10	132.38	44.16	-7.82
IR-Cones	205.07	514.78	464.93	339.25	232.24	133.43	70.30